Commensuration torques and lubricity in double moiré systems

Nicolas Leconte,[1] Youngju Park,[1] Jiaqi An,[1] and Jeil Jung[1,2,*]
[1]*Department of Physics, University of Seoul, Seoul 02504, Korea*
[2]*Department of Smart Cities, University of Seoul, Seoul 02504, Korea*

(Received 29 June 2023; revised 11 April 2024; accepted 17 June 2024; published 22 July 2024)

We study the commensuration torques and layer sliding energetics of twisted trilayer graphene (t3G) and twisted bilayer graphene on hexagonal boron nitride (t2G/BN) that have two contiguous superposed moiré interfaces. Lattice relaxations for typical graphene twist angles of $\sim 1^\circ$ in t3G or t2G/BN are found to break the out-of-plane layer mirror symmetry, give rise to layer rotation energy local minima dips of the order of $\sim 10^{-1}$ meV/atom at double moiré alignment angles, and have stacking energy minima of comparable magnitude between the next-nearest top-bottom layers. Thus, in t3G, the top and bottom layers tend to align when one twisted interface angle is fixed, whereas in t2G/BN, the alignment of the two moiré patterns favors t2G with $\theta \simeq 1.12^\circ$ near the magic angle when the G/BN interface is rotated at $\theta \simeq 0.56^\circ$. Precedence of rotation over sliding during the moiré commensuration is confirmed for periodic boundary systems where the sliding energy barriers drop to $\sim 10^{-4}$ meV/atom for physical misalignment angles as small as $\sim 0.03^\circ$. For finite graphene flakes of diameter D, we find enhanced friction forces for a wider range of angles $\Delta\theta_{\mathrm{FWHM}} \sim C/D$ both near the zero alignment angle in t2G and commensurate double moiré angles in t3G.

DOI: 10.1103/PhysRevB.110.024109

I. INTRODUCTION

Double moiré or supermoiré 2D materials [1–9], have two interfering moiré interfaces due to twist angles or lattice constant mismatch. These double interface systems are often assumed to form commensurate double moiré geometries. An important example in the context of flat band superconductivity is twisted trilayer graphene (t3G) with a twisted middle layer [10–19], and likewise commensurate double moiré geometries have been assumed when studying twisted bilayer graphene on hexagonal boron nitride (t2G/BN) where a spontaneous anomalous Hall effect was measured [20–25]. However, the assumption that equal period and angle aligned commensurate double moiré systems are energetically favored over incommensurate double moiré systems has not been yet confirmed.

In this article, we analyze the atomic structure of double moiré van der Waals materials taking t3G and t2G/BN as prototypical examples to show that torques tend to lock the systems into commensurate double moiré patterns and favor a specific sliding geometry between the alternating layers, generally accompanied by mirror symmetry breaking layer corrugations. We find that the specific sliding atomic structures between the top and next nearest layer only matters when the moiré patterns are commensurate, whereas the sliding energies become practically constant for incommensurate double moiré patterns, similar to the superlubric behavior in single moiré twisted graphene systems studied in the literature [2,26–31].

*Contact author: jeiljung@uos.ac.kr

II. SYSTEMS AND METHODS

The representative double moiré systems considered, namely t3G and t2G/BN, are illustrated in Fig. 1(a), where the layer numerals 1, 2, and 3 correspond to bottom, middle, and top layers, respectively, where θ_{12} and θ_{32} are the twist angles of the bottom and top layers with respect to the reference middle layer. The atomic structure relaxation is carried out using LAMMPS [32] with computational details provided in the Appendix including the indices that specify double moiré supercells in Table I, where we expand the approaches outlined in Refs. [33,34]. The stability of the atomic structure relies on the total energy given as the sum

$$E_{\mathrm{tot}} = E_{\mathrm{el}} + E_{\mathrm{pot}} \tag{1}$$

where we can distinguish the elastic energy $E_{\mathrm{el}} = \sum_i E^i_{\mathrm{el}}/2$ that resists the deformation due to the strains, and the potential energy $E_{\mathrm{pot}} = \sum_i E^i_{\mathrm{pot}}/2$ giving rise to the moiré strain patterns, where the division by 2 accounts for double counting. The local elastic E^i_{el}, potential E^i_{pot}, and interface $E^i_{\mathrm{IF}_{\mathrm{mn}}}$ energies are defined as

$$E^i_{\mathrm{el}} = \sum_{j \in \text{layer i}} \phi^{ij} \tag{2}$$

$$E^i_{\mathrm{pot}} = \sum_{j \notin \text{layer i}} \phi^{ij} = \sum_{j \in \text{ any layer}} \phi^{ij} - E^i_{\mathrm{el}} \tag{3}$$

$$E^i_{\mathrm{IF}_{\mathrm{mn}}} = \sum_{\substack{j \notin \text{ layer i} \\ j \in \text{ layer n or m,}}} \phi^{ij}_{\mathrm{mn}} \tag{4}$$

where ϕ^{ij} represents the pairwise potentials between atoms i and j. By definition, the interface energy and the potential energy give very similar trends, with the additional advantage

 ©2024 American Physical Society

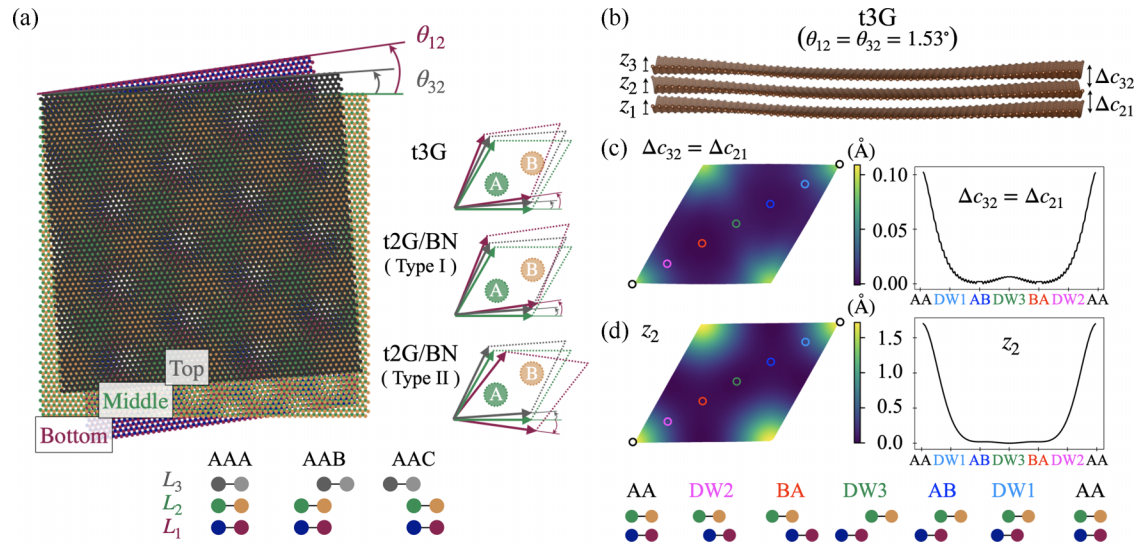

FIG. 1. (a) Double moiré t3G and t2G/BN trilayers with $\theta_{ij} = \theta_i - \theta_j$ twist angles of the i-th layer with respect to the j-th layer. (b) Layer mirror-symmetry breaking corrugations of t3G with $\overline{\text{AAA}}$ top-bottom layer sliding and $\theta_{12} = \theta_{32} = 1.54°$ with moiré length $\lambda_2 = 9.16$ nm. (c) Interlayer distance variations at different local stacking positions and (d) bending corrugations of the middle layer measured from the respective bottom reference layer of the interface.

that for trilayer systems, the interface energy definition allows to focus on a specific interface defined by m and n layers.

In our calculations, the elastic energy contributions in Eq. (2) are about one order of magnitude smaller than the potential and interface energies in Eqs. (3) and (4), and only a small fraction of the total energy in Eq. (1) dictates the stability of our systems. Thus, the interface energies are essentially the potential energies referred to a particular pair of layers. The changes of this interface energy between single moiré (2L) and double moiré (3L) systems can be obtained through

$$\Delta E_{\text{IF}_{mn}}(\boldsymbol{r}) = E^{3L}_{\text{IF}_{mn}}(\boldsymbol{r}) - E^{2L}_{\text{IF}_{mn}}(\boldsymbol{r}), \tag{5}$$

where $E^{3L}_{\text{IF}_{mn}}$ at a given point is obtained relaxing simultaneously all three layers of t3G and then reading the bilayer atomic positions for the considered mn interface, whereas the $E^{2L}_{\text{IF}_{mn}}$ interface energy is obtained using the t2G relaxed atomic positions of the two mn layers that form the interface. In Eq. (5), we have removed the i-index dependence in $E^{i}_{\text{IF}_{mn}}$ in Eq. (4) using instead the position vector $\boldsymbol{r}$ by interpolating the data from the closest i-sublattice points.

Another quantity of interest is the torque constant

$$k_{\pm} = \frac{dE_{\text{tot}}}{d\theta_{32}} \tag{6}$$

that we define as the derivative of the total energy as a function of twist angle, similar to the proposals in Refs. [29,31,35]. Our torque analysis has focused on the rotation of the top layer with respect to the middle layer, where its positive or negative values tend to either reduce or increase the value of θ_{32} toward the commensurate moiré geometry.

III. TWIST DEPENDENT SLIDING LUBRICITY

Here we present the main result of our study, namely that doubly commensurate t3G and t2G/BN moiré systems are more stable than the incommensurate ones. For t3G, we choose three bottom interface angles $\theta_{12} = 1.08°$, $1.54°$, and $2.0°$ to sample the magic angles of alternating twist tNG systems corresponding to $N = 2, 3, \infty$ [36]. Then we rotate the top layer by θ_{32} from $0.1°$ to $2.3°$, with the moiré commensuration being naturally achieved when $\theta_{12} = \theta_{32}$. The relaxed atomic structures generally favor z-axis corrugations breaking layer mirror symmetry, where the typical local stacking-dependent interlayer distance has variation of the order of $\sim$0.1 Å while the middle layer z-axis corrugations are of the order of $\sim$1.75 Å , roughly one half of the average interlayer distance [see Fig. 1(c) and Fig. 1(d)].

The main result of this work, namely the favoring of doubly commensurate angles, is summarized in the twist angle θ_{32} dependent total energies of Fig. 2(a), and select total energies are listed in Table III. Total energy local minima are found at the commensurate angles for all three θ_{12} values considered provided that we allow a bending corrugation as illustrated in Fig. 1(b). In fact, the mirror-symmetric t3G with a completely flat middle layer has a higher total energy compared to the corrugated atomic structure. The binding energies E_b are defined as the difference between the dashed interpolated line using the total energies away from commensuration and the actual total energy at commensuration [see Fig. 2(a) and Fig. 2(b)]. The torques are generally larger for smaller θ_{12} angles, and the signs of the torque constants k_+ and k_- obtained using Eq. (6) will decrease/increase the θ_{32} to bring the incommensurate double moiré systems back to commensuration. In Fig. 2(a), we show that the commensurate double moiré systems are most stable in the $\overline{\text{AAA}}$-sliding, where the overline indicates relative sliding between the layers prior to twisting and the rotation center is located at the A-sublattice site of the bottom layer. In fact, the energy difference between the $\overline{\text{AAA}}$ at the local minima dip and $\overline{\text{AAB}}$ maxima represented is equal to 0.18 meV/atom near $\sim 1°$ and drops to 0.06 meV/atom for an angle of $3.47°$ (not shown here) and are comparable to the magnitude of the energy local minima dips due to the

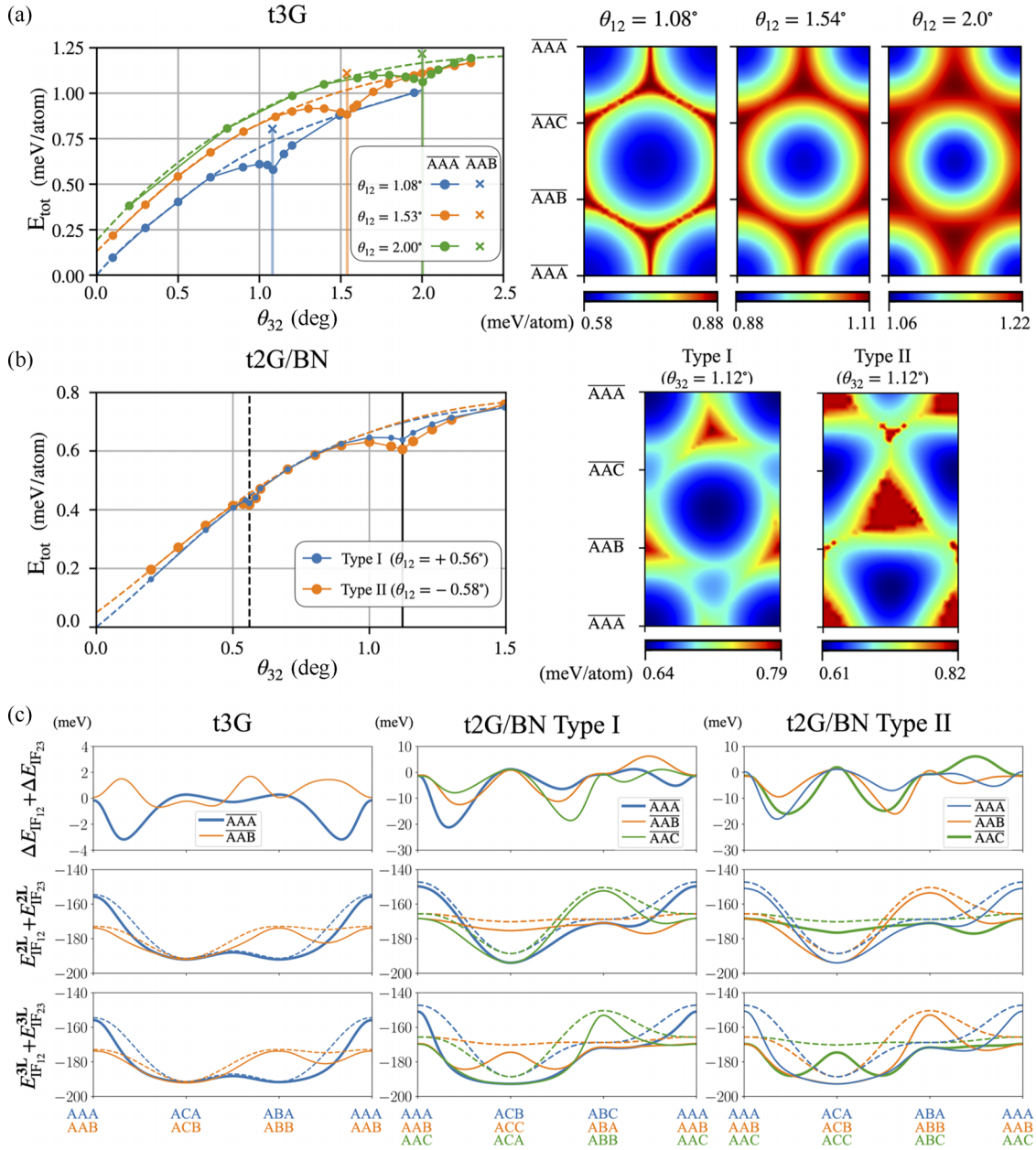

FIG. 2. (a) Total energies of t3G double moiré systems for three different values of θ_{12} where θ_{32} is varied from ∼0.1° to ∼2.3°. The commensurate $\theta_{12} = \theta_{32}$ angles are indicated by vertical lines have a local energy dip. The x-symbols represent the $\overline{\text{AAB}}$ sliding and the dashed lines are interpolated through a third degree polynomial. On the right-hand side, we show total energies for different sliding of the top layer for select commensurate angles $\theta_{12} = \theta_{32}$. These colormaps indicate which sliding configuration is the most stable and allow us to extract the sliding energy that we can contrast with the rotation energies. (b) Similar plots for t2G/BN (Type I and Type II) where local minima are found for two different values of θ_{32}, corresponding to $L_{12} = L_{32}$ (solid vertical line) and $L_{12} = L_{32}/2$ (dashed vertical line). (c) Interpolated interface energy differences $\Delta E_{\text{IF}_{\text{mn}}}(\boldsymbol{r})$ of Eq. (5) illustrating the local energy gain/penalty when a single moiré comes into contact with a second moiré interface, plotted along a straight line that connects the opposite diagonal corners of the moiré cell. The most stable stacking arrangement is highlighted with a thicker line. The negative energies correspond to a stabilizing gain in energy, whereas positive energies indicate a destabilizing energy penalty.

rotation. Our sliding dependent total energy plots in both $x - y$ directions indicate that there are barrier-free sliding paths leading to the global minimum at $\overline{\text{AAA}}$-sliding [36,37]. Similar conclusions follow for t2G/BN where we fix the substrate angle between G and hBN at $\theta_{12} = 0.56°$ for type I or $-0.58°$ for type II. We allow θ_{32} between both graphene layers to change up to a value of 1.5° to achieve moiré periods that satisfy $pL^M_{tBG} = q\,L^M_{tGBN}$, where p, q are integers [38]. For $p = 1$, we observe two local minima dips in the energy curve corresponding to $\theta_{32} = 0.56°$ for $q = 2$ with a G/G moiré

pattern period twice as large as that of the G/BN interface, and $\theta_{32} = 1.12^\circ$ for equal periods with $q = 1$. The double moiré commensuration total energy local minima dips in Fig. 2(a) and Fig. 2(b) for t3G and t2G/BN due to interfering moiré patterns can be further understood through the interface energy difference between three-layer and two-layer relaxed systems, calculated using Eq. (5) and illustrated as line plots in Fig. 2(c), which shows the energy gain/penalty (negative and positive values, respectively) arising when two moiré patterns interfere with each other. The strongest local energy penalties often happen away from the high symmetry local stacking regions and the global energy minimization does not follow simple rules of thumb, especially for heterostructures like t2G/BN.

IV. TWIST DEPENDENT SLIDING LUBRICITY

To further understand the twist angle dependent sliding energetics and frictions in relation to the stabilization of the commensurate double moiré systems versus the incommensurate ones, we show in Fig. 3 the local stacking distribution maps for each one of the t3G interfaces. For commensurate moiré patterns and stable $\overline{\text{AAA}}$-sliding, the energetically unfavorable AA local stacking that makes about 7.7% of the total area increases to 12.2% for the less stable $\overline{\text{AAB}}$-sliding. We approximate the incommensurate double moiré systems by allowing two different moiré pattern periods, such as the combination of $1.54^\circ - 1.1^\circ$ with 1/7 moiré length ratios or $1.54^\circ - 1.5^\circ$ with 1/39 ratios. For these geometries, the relative distribution of the AA, AB, or BA local stacking areas become practically insensitive to the relative sliding of the top layer resulting in almost the same local stacking area ratios for both $\overline{\text{AAA}}$ and $\overline{\text{AAB}}$ slidings, indicating in turn that they will have weak interlayer sliding force gradients. Sliding energy landscapes of 10^{-1} meV/atom for commensurate double moiré systems where $\Delta\theta = \theta_{32} - \theta_{12} = 0^\circ$ quickly drops to $10^{-4} \sim 10^{-5}$ meV/atom for small twist angles away from commensuration of $\Delta\theta \simeq 0.03^\circ \sim 0.5^\circ$ suggesting moiré superlubricity away from double moiré commensuration. Therefore, the sliding-dependent energy landscape of the outer layers will have non-negligible gradients for locally commensurate double moiré patterns.

To assess these interlayer sliding forces in a more realistic setting, we perform friction force calculations based on flakes in Fig. 4 and obtain the friction coefficients $\mu = \overline{|\boldsymbol{F}_f|}/F_n$ as the ratio of the friction force amplitude integrated along half a period τ of the armchair direction of the unrotated reference layer when we apply a constant normal force $F_n = 1$ nN/atom [39]. We note that superlow friction is usually defined as the dynamic friction coefficient being lower than $\mu = 0.01$ or close to $\mu = 0.001$ at the limit of what can be detected by available tribometers [40], where our quasistatic coefficient values should be considered as upper bounds to the dynamic values [41]. Using $D = 20$ nm flakes, it was shown experimentally that the friction coefficient for t2G drops into the superlubric regime away from zero alignment [28]. For our t3G systems, the commensurate configuration at 1.54° has a friction coefficient of about 25% of the aligned t2G value

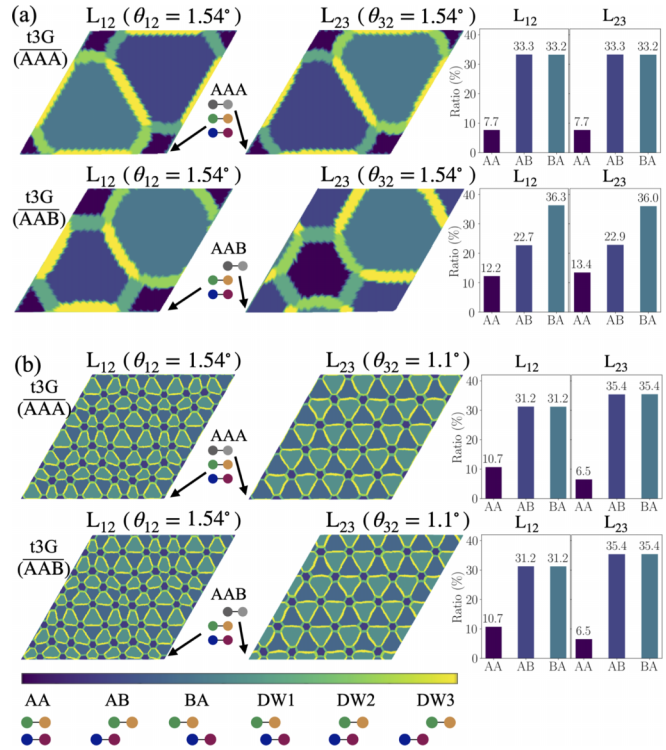

FIG. 3. Local stacking rearrangement due to lattice relaxations in double moiré t3G systems using the conventions of Ref. [33]. These maps visualize the assignment of a high-symmetry stacking (AA, AB, BA,...) to each one of the intermediate stackings that are naturally present in moiré systems that facilitates quantifying the lattice reconstruction and making comparisons between systems. (a) Commensurate double moiré patterns with equal angles $\theta_{12} = \theta_{32} = 1.54^\circ$ for two top-bottom layer sliding geometries. The $\overline{\text{AAA}}$ sliding shows a smaller AA local stacking area when compared with the $\overline{\text{AAB}}$ sliding going from 7.7% to 12.2%, respectively. (b) Incommensurate double moiré patterns approximated by commensurate approximants in a system with unequal angles $\theta_{12} = 1.54$ and $\theta_{32} = 1.1^\circ$ and corresponding local stacking area ratios for two sliding geometries. Although the relaxation profiles change with different sliding geometries, the ratios for local AA, AB, and BA stackings remain nearly the same.

and transitions into the superlubric regime away from double moiré commensuration, where $\Delta\theta_{\text{FWHM}} \sim C/D^\circ$ is the width of the friction peak that can be fit with $C \sim 0.04$ deg · nm for both single moiré t2G and double moiré t3G. The suppressed friction in t3G near $\theta_{32} = 0^\circ$ likely results from allowing relaxations in the unconstrained middle layer while in the t2G simulations the bottom layer is kept rigid. The computation details as well as further discussions in terms of the flake size are given in the Appendix.

V. DISCUSSIONS

We have shown that double moiré systems tend to align their angles and form rational p/q moiré length ratios, as illustrated in alternating t3G $p = q = 1$ and t2G/BN $p = 1$, $q = 1, 2$ systems, with the effect diminishing quickly for p, q

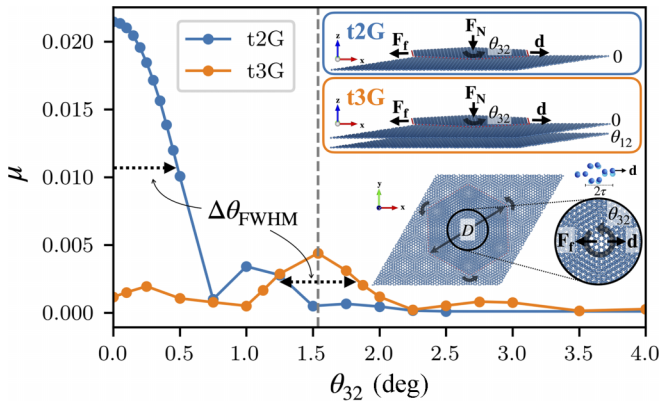

FIG. 4. Friction coefficients $\mu = \overline{|\boldsymbol{F}_f|}/F_n$ for t2G and t3G calculated using $F_n = 1$ nN/atom with a rigid tip and bottom layer. We see a clear transition from the incommensurate superlubric to sizable friction regime near zero angle commensuration in single interface t2G and the supermoiré double interface commensuration at 1.54° in t3G. The double moiré frictions are about 1/4 of the single moiré counterpart. The sizable friction angle range follows $\Delta\theta_{\mathrm{FWHM}} \sim 0.04°/D$ where D(nm) is the flake diameter.

values larger than 1. The binding energies gained during the rotational alignment near $\theta_{32} \simeq 1°$, 1.5°, and 2° of the order of ∼0.2, 0.17, and 0.13 meV/atom, respectively, are comparable in magnitude with the energy differences resulting from the relative sliding of the top and bottom layers in commensurate double moiré geometries [36,37]. The suppression of sliding energies by a few orders of magnitude for incommensurate double moiré geometries happens in periodic systems as soon as the system is marginally twisted away from double moiré commensuration with very small physical rotation angles as small as ∼0.03°. This observation on double moiré systems extends previous knowledge from single moiré systems where zero degree alignment was shown to prevent superlubricity due to the increased number of energy barriers the system has to overcome when compared to the incommensurate configurations where friction forces cancel out on average for sufficiently hard periodic materials [42]. Simulations based on finite flakes indicate sizable finite friction forces for wider twist angle deviations of $\Delta\theta_{\mathrm{FWHM}} \simeq 2°$ in a flake with a diameter $D = 20$ nm. These results indicate precedence of rotational alignment over the relative sliding of top-bottom layers in the double commensuration process. Thus, commensurate double moiré local domains are expected within long period incommensurate double moiré systems akin to the commensurate stacking domains found in marginally t2G [43], suppressing the angle disorder prevalent in t2G. In future work, one could consider additional contributions to the friction, such as the nature of a possible substrate, the dry or wet environment of the measurements, and electronic excitation contributions [44,45] that may further affect the current results.

The torque calculations in t3G suggest that after fixing the bottom interface angle θ_{12} in experiments targeting θ_{32} angles that are equal or slightly larger than the commensurate double moiré angle will more easily tend to lock the system into moiré commensuration, whereas targeting a smaller angle may result in the system rotating back to the trivial zero-alignment commensurate phase upon thermal annealing. Our results for t2G/BN suggest that it is possible to prepare t2G at an angle θ that is defined by the angle formed by G with the underlying h/BN substrate, by exploiting double moiré commensuration. G/hBN samples at an angle of 0.56° might preferably host magic angle tBG. The qualitative conclusions based on the t3G and t2G/BN double moiré systems found in this work are expected to apply for a variety of other twisted layered van der Waals materials forming multiple moiré patterns.

ACKNOWLEDGMENTS

We thank X. Gao and O. Hod for helpful discussions on the calculations of the friction forces. This work was supported by the Basic Study and Interdisciplinary R&D Foundation Fund of the University of Seoul (2022) (J.J.). We also acknowledge funding from the Korean NRF through the Grant No. RS-2023-00249414 (N.L.).

APPENDIX A: COMPUTATIONAL DETAILS

We use the REBO2 force field [46] for the intralayer interactions of graphene and EXTEP [47] for those of hexagonal boron nitride, whose equilibrium geometries are $a_{\mathrm{G}} = 2.4602$ Å and $a_{\mathrm{BN}} = 2.50576$ Å, respectively. The interlayer force fields are based on EXX-RPA-informed [48] DRIP [49] parameterizations [50] and we used both the *fire* and *CG* minimization scheme [51] with a timestep of 0.0001 ps for the former and 0.001 ps for the latter and a stopping tolerance on the forces of 10^{-5} eV/Å.

Commensurate moiré superlattices can be built in general based on 4 integer indices using the conventions in Ref. [34], as exemplified in Ref. [33] for t2G systems. For double moiré systems, the same approach requires the definition of 6 integers, namely (i, j, i', j', i'', j''). These integers define the following three transformation matrices where $\boldsymbol{M}_i$ with $i = 1, 2, 3$ correspond to L_1, L_2, and L_3, respectively:

$$\boldsymbol{M}_1 = \begin{pmatrix} i & j \\ -j & i+j \end{pmatrix},$$
$$\boldsymbol{M}_2 = \begin{pmatrix} i' & j' \\ -j' & i'+j' \end{pmatrix}, \tag{A1}$$
$$\boldsymbol{M}_3 = \begin{pmatrix} i'' & j'' \\ -j'' & i''+j'' \end{pmatrix}.$$

These matrices relate the lattice vectors $\boldsymbol{r}_1$ and $\boldsymbol{r}_2$ to the lattice vectors $\boldsymbol{a}_1$ and $\boldsymbol{a}_2$ of the respective layers through

$$\begin{pmatrix} \boldsymbol{r}_1 \\ \boldsymbol{r}_2 \end{pmatrix} = \boldsymbol{M}_1 \cdot \begin{pmatrix} \boldsymbol{a}_1 \\ \boldsymbol{a}_2 \end{pmatrix} = \boldsymbol{M}_2 \cdot \begin{pmatrix} \boldsymbol{a}'_1 \\ \boldsymbol{a}'_2 \end{pmatrix} = \boldsymbol{M}_3 \cdot \begin{pmatrix} \boldsymbol{a}''_1 \\ \boldsymbol{a}''_2 \end{pmatrix} \tag{A2}$$

TABLE I. Torque constants $k_\pm = dE_{\rm tot}/d\theta_{32}$ in units of meV/(atom · rad) as defined in Eq. (6) evaluated to the left (k_-) and right (k_+) of the respective local minima at the commensurate angles θ_{32}, and the binding energy $E_b(\theta_{32})$ estimated as the difference between the smoothly interpolated polynomial curve and the respective minima in Fig. 2(a) and Fig. 2(b).

	t3G			t2G/BN			
		$(\theta_{12}=\theta_{32})$		Type I $(\theta_{12}=+0.56^\circ)$		Type II $(\theta_{12}=-0.58^\circ)$	
θ_{32} (°)	1.08	1.54	2.00	0.56	1.12	0.56	1.12
$k_-(\theta_{32})$	−42.12	−18.34	−8.513	−40.01	−9.69	−7.124	−14.33
$k_+(\theta_{32})$	75.06	53.04	36.85	48.01	35.52	54.54	40.46
$E_b(\theta_{32})$	0.156	0.135	0.104	0.024	0.058	0.039	0.095

The lattice mismatch $\alpha_{\rm mn}$ and twist angle $\theta_{\rm mn}$ between the layers m and n can be related to these integers as follows:

$$\begin{aligned}
\alpha_{12} &= \frac{|\boldsymbol{a}_1|}{|\boldsymbol{a}'_1|} = \sqrt{\frac{i'^2+j'^2+i'j'}{i^2+j^2+ij}},\\
\alpha_{32} &= \frac{|\boldsymbol{a}''_1|}{|\boldsymbol{a}'_1|} = \sqrt{\frac{i'^2+j'^2+i'j'}{i''^2+j''^2+i''j''}},\\
\theta_{12} &= \theta_1-\theta_2 = \cos^{-1}\left[\frac{2ii'+2jj'+ij'+ji'}{2\alpha_{12}(i^2+j^2+ij)}\right],\\
\theta_{32} &= \theta_3-\theta_2 = \cos^{-1}\left[\frac{2i''i'+2j''j'+i''j'+j''i'}{2\alpha_{32}(i''^2+j''^2+i''j'')}\right],
\end{aligned} \tag{A3}$$

where we assume the middle L_2 layer as the untwisted reference layer. In Table II, we summarize the six integers used to generate the systems represented in Fig. 2(a) and Fig. 2(b) in the main text for the t3G and the two t2G/BN systems.

In Table III, we show the total energies and their breakdown for representative doubly commensurate geometries of t3G and t2G/BN.

In Eqs. (1)–(4) from the main text, we formally introduced how the different energy contributions are defined. These expressions are valid for pairwise potentials. More generally, if one performs DFT calculations, one can also extract such contributions. Similar to what we do here under the hood to separate the elastic and potential contributions, i.e., (i) calculate the total energy for the full system, (ii) calculate separately the energy for the relaxed layers (elastic contribution), and (iii) obtain the potential energy by subtracting the elastic contribution from the total energy, in DFT, the binding energy which can be related to our potential here is often also calculated in a similar manner (possibly accounting for the Basis Set Superposition Error [52]). Alternatively, the DFT elastic energy can also be obtained from the displacement of the atoms using the expressions given in Ref. [53] where the Lame parameters for different force fields/DFT schemes were calculated/reminded in Ref. [33].

APPENDIX B: T2G ANGLE-DEPENDENT ENERGIES

In the main text, we estimated the double moiré commensuration energies by comparing the actual calculations against the interpolated data near double commensuration obtained based on the energies outside this region. In the following, we show in Fig. 5 the twist angle dependent total energy of t2G for different atomic relaxation schemes.

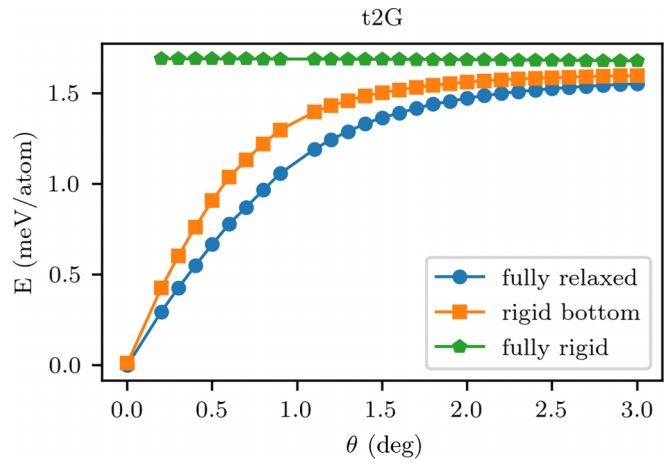

FIG. 5. Twist angle dependence of the total energies per atom for t2G when the two layers are fully relaxed (blue), when the bottom layer atoms are kept fixed (orange), and where both layers are rigid and kept at a constant interlayer distance of 3.35 Å. The system favors the zero degree alignment by ∼1.5 meV/atom when we allow atomic relaxations.

APPENDIX C: TORQUE MAPS

We illustrate in Fig. 6 the difference between the local torque maps for a commensurate and an incommensurate moiré system calculated through

$$\boldsymbol{\tau}_s = (\boldsymbol{r}_s - \boldsymbol{r}_{cm}) \times \boldsymbol{F}_s, \tag{C1}$$

where s is the sublattice index and cm refers to the center of mass of the dimer formed by the neighboring A and B sublattices, and where $\boldsymbol{F}_s$ is the interface component of the force acting on an atom extracted at the end of the LAMMPS minimization by subtracting the intralayer forces. The left panels show the local torque maps for commensurate moiré pattern cases where the moiré cell has been repeated 15 times for a more direct comparison with the right-hand panels that have the same size. On the right panel, we illustrate the same torques for an incommensurate moiré configuration modeled through a commensurate cell approximant containing multiple moiré repetitions with a longer supermoiré period. In the middle layer, L_2, we see that a large region of the atoms feels the same torque as is seen for the commensurate phase, suggesting that within the region confined by long-period triangular patches we largely recover the commensurate moiré phase behavior seen for $\theta_{23} = 1.54^\circ$.

APPENDIX D: FRICTION CALCULATIONS

We extend here the calculations of the friction forces when applying a normal force F_N of 1 nN, for the reference t2G system and the t3G system with $\theta_{12} = 1.54^\circ$ using the quasistatic approach outlined in Refs. [54–56] where the static lateral forces are calculated for a series of intermediate positions

TABLE II. Details about the commensurate cells that are used for our simulations on the t3G and t2G/BN systems where the first column contains θ_{12}, the second column summarizes the θ_{32} for each of the corresponding θ_{12} values, the third column contains the six integers as defined in Refs. [33,34] where the first two integers control the lattice vectors of the first layer, the next two integers define the lattice of the second layer and the final two integers orient the lattice vectors of the top layer following Eq. (A2). The fourth column contains the slightly strained lattice constant a_{L_3} for the third layer which is different from the unstrained lattice constants of 2.4602 Å for L_1 and L_2. The fifth column contains the number of atoms and the final column represents the super-moiré length or commensuration cell length λ as a multiple of the commensurate cell moiré length λ_i when $\theta_{12} = \theta_{32}$, where $\lambda_1 = 129.97$ Å, $\lambda_2 = 91.62$ Å and $\lambda_3 = 70.32$ Å for $\theta_{12} = 1.0845^\circ$, 1.5385° and 2.0046° respectively for t3G and $\lambda_4 = \lambda_5 = 125.71$ Å for t2G/BN Type I and t2G/BN Type II. We highlight the commensurate angle configurations from the main text in bold while the other entries are commensurate approximations of the incommensurate angle combinations.

t3G

θ_{12} (deg)	θ_{32} (deg)	$(i\ j\ i'\ j'\ i''\ j'')$	a_{L_3}(Å)	# atoms	λ
1.084549	0.098591	341 330 330 341 331 340	2.460226	2026246	$11\lambda_1$
	0.299180	899 870 870 899 878 891	2.460278	14083050	$29\lambda_1$
	0.500560	403 390 390 403 396 397	2.460300	2829990	$13\lambda_1$
	0.699713	961 930 930 961 950 941	2.460291	16092466	$31\lambda_1$
	0.898632	1085 1050 1050 1085 1079 1056	2.460253	20513502	$35\lambda_1$
	1.049565	961 930 930 961 960 931	2.460204	16092846	$31\lambda_1$
	1.084549	**31 30 30 31 31 30**	**2.460190**	**16746**	$\boldsymbol{\lambda_1}$
	1.150275	1023 990 990 1023 1025 988	2.460162	18236534	$33\lambda_1$
	1.200741	868 840 840 868 871 837	2.460138	13129050	$28\lambda_1$
	1.491197	248 240 240 248 251 237	2.459963	1071810	$8\lambda_1$
	1.951946	155 150 150 155 159 146	2.459556	418722	$5\lambda_1$
1.538500	0.099248	682 651 651 682 653 680	2.460244	7997326	$31\lambda_2$
	0.299135	792 756 756 792 763 785	2.460329	10784906	$36\lambda_2$
	0.498959	814 777 777 814 789 802	2.460384	11392218	$37\lambda_2$
	0.699314	242 231 231 242 236 237	2.460410	1006902	$11\lambda_2$
	0.901887	638 609 609 638 626 621	2.460405	6998394	$29\lambda_2$
	1.098945	154 147 147 154 152 149	2.460371	407758	$7\lambda_2$
	1.201971	704 672 672 704 697 679	2.460342	8521378	$32\lambda_2$
	1.301824	286 273 273 286 284 275	2.460305	1406374	$13\lambda_2$
	1.398649	242 231 231 242 241 232	2.460263	1006942	$11\lambda_2$
	1.499055	858 819 819 858 857 820	2.460212	12657686	$39\lambda_2$
	1.538500	**22 21 21 22 22 21**	**2.460190**	**8322**	$\boldsymbol{\lambda_2}$
	1.577943	858 819 819 858 859 818	2.460167	12657842	$39\lambda_2$
	1.600032	550 525 525 550 551 524	2.460153	5201302	$25\lambda_2$
	1.700421	418 399 399 418 420 397	2.460087	3004326	$19\lambda_2$
	1.794869	132 126 126 132 133 125	2.460018	299606	$6\lambda_2$
	1.900421	374 357 357 374 378 353	2.459932	2405226	$17\lambda_2$
	1.999934	220 210 210 220 223 207	2.459844	832278	$10\lambda_2$
2.004628	0.200433	170 160 160 170 161 169	2.460326	490182	$10\lambda_3$
	0.801831	255 240 240 255 246 249	2.460551	1102842	$15\lambda_3$
	1.202796	255 240 240 255 249 246	2.460551	1102842	$15\lambda_3$
	1.397199	561 528 528 561 551 538	2.460508	5337818	$33\lambda_3$
	1.603742	85 80 80 85 84 81	2.460431	122542	$5\lambda_3$
	1.700933	561 528 528 561 556 533	2.460384	5337998	$33\lambda_3$
	1.799055	663 624 624 663 659 628	2.460329	7455662	$39\lambda_3$
	1.899139	323 304 304 323 322 305	2.460265	1769586	$19\lambda_3$
	1.950459	629 592 592 629 628 593	2.460230	6710766	$37\lambda_3$
	2.004628	**17 16 16 17 17 16**	**2.460190**	**4902**	$\boldsymbol{\lambda_3}$
	2.056017	663 624 624 663 664 623	2.460150	7456022	$39\lambda_3$
	2.100064	357 336 336 357 358 335	2.460115	2161826	$21\lambda_3$
	2.198572	527 496 496 527 530 493	2.460030	4711026	$31\lambda_3$
	2.301520	459 432 432 459 463 428	2.459934	3573806	$27\lambda_3$

TABLE II. (*Continued*.)

t2G/BN Type I

θ_{12} (deg)	θ_{32} (deg)	(i j i' j' i'' j'')	a_{L_3}(Å)	# atoms	λ
0.560656	0.200227	812 812 812 840 817 835	2.460259	12143930	$28\lambda_4$
	0.400464	406 406 406 420 411 415	2.460298	3035950	$14\lambda_4$
	0.501637	1102 1102 1102 1140 1119 1123	2.460306	22366846	$38\lambda_4$
	0.546279	1131 1131 1131 1170 1150 1151	2.460308	23559530	$39\lambda_4$
	0.560656	**58 58 58 60 59 59**	**2.460308**	**61958**	$\mathbf{2}\lambda_4$
	0.583082	725 725 725 750 738 737	2.460308	9680938	$25\lambda_4$
	0.600704	812 812 812 840 827 825	2.460307	12143770	$28\lambda_4$
	0.700824	232 232 232 240 237 235	2.460300	991330	$8\lambda_4$
	0.800943	203 203 203 210 208 205	2.460286	758990	$7\lambda_4$
	0.897056	145 145 145 150 149 146	2.460265	387242	$5\lambda_4$
	1.000094	1073 1073 1073 1110 1106 1077	2.460235	21205546	$37\lambda_4$
	1.079783	783 783 783 810 809 784	2.460207	11292158	$27\lambda_4$
	1.121311	**29 29 29 30 30 29**	**2.460190**	**15490**	$\boldsymbol{\lambda}_4$
	1.159974	841 841 841 870 871 840	2.460173	13027150	$29\lambda_4$
	1.229816	899 899 899 930 933 896	2.460140	14886094	$31\lambda_4$
	1.300703	725 725 725 750 754 721	2.460103	9681482	$25\lambda_4$
	1.495028	261 261 261 270 273 258	2.459981	1254762	$9\lambda_4$
	1.761923	203 203 203 210 214 199	2.459767	759098	$7\lambda_4$
	2.018092	145 145 145 150 154 141	2.459512	387322	$5\lambda_4$

t2G/BN Type II

θ_{12} (deg)	θ_{32} (deg)	(i j i' j' i'' j'')	a_{L_3}(Å)	# atoms	λ
−0.579874	0.200227	840 784 840 812 835 817	2.460259	12145498	$28\lambda_5$
	0.537294	1440 1344 1440 1392 1417 1415	2.460308	35692418	$48\lambda_5$
	0.560656	**60 56 60 58 59 59**	**2.460308**	**61966**	$\mathbf{2}\lambda_5$
	0.584017	1440 1344 1440 1392 1415 1417	2.460308	35692418	$48\lambda_5$
	0.600704	840 784 840 812 825 827	2.460307	12145338	$28\lambda_5$
	0.700824	240 224 240 232 235 237	2.460300	991458	$8\lambda_5$
	0.800943	210 196 210 203 205 208	2.460286	759088	$7\lambda_5$
	0.897056	150 140 150 145 146 149	2.460265	387292	$5\lambda_5$
	1.000094	1110 1036 1110 1073 1077 1106	2.460235	21208284	$37\lambda_5$
	1.079783	810 756 810 783 784 809	2.460207	11293616	$27\lambda_5$
	1.121311	**30 28 30 29 29 30**	**2.460190**	**15492**	$\boldsymbol{\lambda}_5$
	1.159974	870 812 870 841 840 871	2.460173	13028832	$29\lambda_5$
	1.229816	930 868 930 899 896 933	2.460140	14888016	$31\lambda_5$
	1.300703	750 700 750 725 721 754	2.460103	9682732	$25\lambda_5$
	1.495028	270 252 270 261 258 273	2.459981	1254924	$9\lambda_5$
	1.761923	210 196 210 203 199 214	2.459767	759196	$7\lambda_5$
	2.018092	150 140 150 145 141 154	2.459512	387372	$5\lambda_5$
	2.099900	1530 1428 1530 1479 1434 1574	2.460238	40294166	$51\lambda_5$
	2.299955	1470 1372 1470 1421 1369 1521	2.460025	37197972	$49\lambda_5$

when dragging a hexagonal flake along an infinite substrate as illustrated in Fig. 4 in the main text. In our calculations, we assume for the top flake a rigid geometry with variable interlayer distance upon which we apply a constant normal force. We then evaluate the magnitude of the lateral friction force along the x-direction corresponding to the armchair direction of the unrotated reference layer. The friction forces entering the definition of the friction coefficients are sometimes taken as the maximum or the integrated force along this pulling direction. In our case, we use the integrated value of the lateral force for half-period of the supercell along the armchair sliding direction. We keep the bottom layer fixed throughout the calculations while sliding the top layer. For this specific set of calculations, we use the *cg* and *fire* algorithms consecutively using a common timestep of 0.001 ps where their respective stopping criterion are set to 10^{-18} eV on the total energies for the former and 5×10^{-3} eV/Å on the forces for the latter. We note that unlike for the calculations for the main text where the top layer atoms are allowed to relax for each of the high symmetry stacking configurations, we do not relax them here for each intermediate stacking, as a first approximation. The main observation in Fig. 7 is that, indeed, the t3G system transitions into superlubricity when twisted away from double commensuration at 1.54° by looking at the friction forces obtained by integrating the friction force over half a period τ of the armchair direction of the unrotated reference layer. We

TABLE III. Sliding dependent total, elastic, and interface energies for $\theta_{12} = \theta_{32} = 1.5385^\circ$ for t3G, $\theta_{12} = 0.56^\circ, \theta_{32} = 1.12^\circ$ for t2G/BN-I, and $\theta_{12} = -0.58^\circ, \theta_{32} = 1.12^\circ$ for t2G/BN-II for systems containing 8322, 15490, and 15492 atoms, respectively. These numbers are used to renormalize and report the energies in eV/atom. We note that the mirror-symmetric (ms) geometry has a higher total energy by 0.03 meV/atom than the lowest energy geometry.

	E_{tot}	E_{el}	E_{IF12}	E_{IF23}
t3G ($\overline{AAA}$)	−7.42537	−7.39458	−0.01542	−0.01541
t3G ($\overline{AAA}$, ms)	−7.42534	−7.39459	−0.01538	−0.01538
t3G ($\overline{AAB}$)	−7.42510	−7.39471	−0.01521	−0.01516
t2G/BN-I ($\overline{AAA}$)	−7.19472	−7.16454	−0.01458	−0.01559
t2G/BN-I ($\overline{AAB}$)	−7.19451	−7.16466	−0.01442	−0.01542
t2G/BN-I ($\overline{AAC}$)	−7.19467	−7.16455	−0.01456	−0.01556
t2G/BN-II ($\overline{AAA}$)	−7.19561	−7.16554	−0.01452	−0.01556
t2G/BN-II ($\overline{AAB}$)	−7.19562	−7.16553	−0.01453	−0.01556
t2G/BN-II ($\overline{AAC}$)	−7.19581	−7.16556	−0.01463	−0.01563

confirmed that this short period suffices to capture the main trends reported here. This is clearest when looking at the $D = 20$ nm curve. The full width at half maximum (FWHM) of its friction peak equals 0.8°. When contrasting these results with the ones from the reference t2G system, we note that the maximum of the friction peak of t3G is about 25% the size of the maximum of the peak for t2G. The FWHM of the t2G case is similar but slightly larger than the one from t3G, namely 0.94°. We note that based on additional calculations on t2G, there exists a linear scaling between

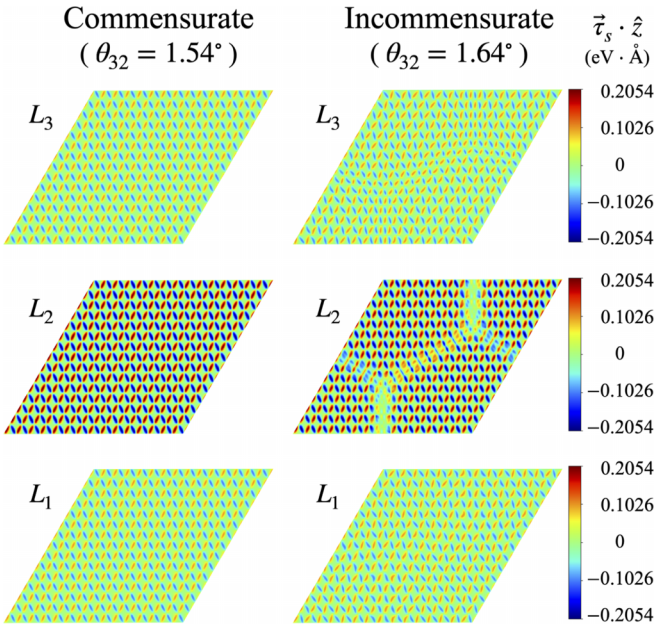

FIG. 6. Local torque $\boldsymbol{\tau}_s$ defined in Eq. (A1) for each layer in t3G at the site $i \in$ sublattice s are illustrated when the two moiré interfaces are commensurate ($\theta_{12} = \theta_{32} = 1.54^\circ$) (left) and incommensurate ($\theta_{12} = 1.54^\circ$, $\theta_{32} = 1.64^\circ$) (right). We observe the presence of a supermoiré pattern with a longer period for the incommensurate moiré case that gives rise to the total energy differences with respect to the doubly commensurate moiré case.

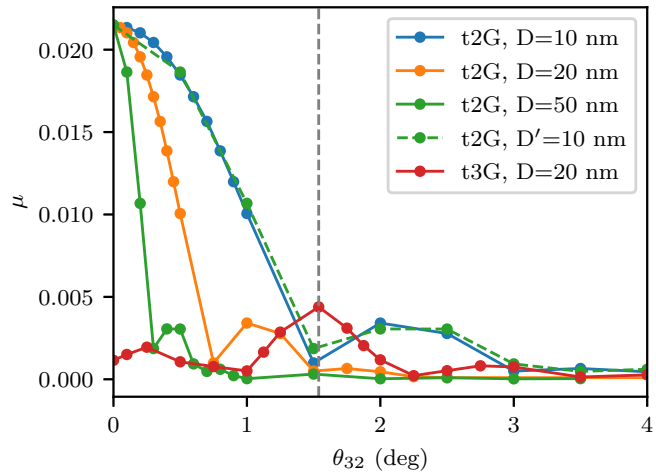

FIG. 7. Friction coefficients for t2G and t3G using the flake geometry illustrated in the main text showing the flake's diameter dependence of the transition into the frictionless regime. The larger the flake, the narrower the friction peak becomes.

the diameter of the flake and the width of the peak where the width of the peak decreases with increasing diameter. For instance, when multiplying the x-coordinates from the $D = 50$ nm by 5 (dashed green curve indicated by $D' = 10$ nm), we overlay almost exactly the $D = 10$ nm curve (solid blue curve). Applying this same linear scaling procedure, we note that we can capture the width from the experimental friction peak from Ref. [28] when setting $D = 2.9$ nm, which agrees quantitatively with the size of the experimental tip whose diameter is estimated to be between 1.7 and 3.0 nm. We finally note that these simplified friction calculations using only two or three layers only give a qualitative idea in terms of the amplitude of the friction forces. More realistic results can be achieved by including additional layers to simulate the sliding tip to allow for more realistic relaxation effects. We note, for instance, that the t2G system can lead to stick-slip behavior when the tip is sufficiently soft [28]. Such a condition can be approximated by contacting the top layer with a spring whose spring constant can be controlled while letting the top layer atoms freely relax [28]. Our simulation conditions then correspond to a very stiff spring.

The analysis we have presented far relied on free-standing trilayer systems. To assess the impact a substrate would have on our results, we have performed the following checks. For t3G, we have checked that adding a rigid hBN substrate layer with a twist angle of 3.41° dampens but does not completely remove the bending corrugation observed for the mirror symmetry broken commensurate case. Indeed, the maximum bending corrugation goes down for the suspended t3G system from 1.70 Å as seen in Fig. 1(d) in the main text to 0.25, 0.35, and 0.45 Å for L_1, L_2, and L_3, respectively, when we add a rigid substrate layer in contact with L_1. If we do not fix the additional substrate layer, the bending corrugation actually increases by up to 3.79 Å, hence a realistic substrate simulation involving many more layers [36,57] would probably give a maximum bending corrugation somewhere in the middle of those two values. For t2G on hBN, we have checked that adding a fixed aligned hBN

substrate in AA' stacking below the existing hBN layer does not modify the qualitative behaviors and the system still shows local energy dips at the commensurate angles. We thus expect our conclusions based on free-standing systems to hold under more realistic experimental conditions when substrates are present.

[1] N. R. Finney, M. Yankowitz, L. Muraleetharan, K. Watanabe, T. Taniguchi, C. R. Dean, and J. Hone, Nat. Nanotechnol. **14**, 1029 (2019).

[2] W. Wang, J. Shen, and Q.-C. He, Phys. Rev. B **99**, 054103 (2019).

[3] M. Anđelković, S. P. Milovanovic, L. Covaci, and F. M. Peeters, Nano Lett. **20**, 979 (2020).

[4] D. L. Miller, K. D. Kubista, G. M. Rutter, M. Ruan, W. A. de Heer, P. N. First, and J. A. Stroscio, Phys. Rev. B **81**, 125427 (2010).

[5] Z. Wang, Y. B. Wang, J. Yin, E. Tóvári, Y. Yang, L. Lin, M. Holwill, J. Birkbeck, D. J. Perello, S. Xu, J. Zultak, R. V. Gorbachev, A. V. Kretinin, T. Taniguchi, K. Watanabe, S. V. Morozov, M. Andelkovic, S. P. Milovanovic, L. Covaci, F. M. Peeters *et al.*, Sci. Adv. **5**, eaay8897 (2019).

[6] X. Zhang, K.-T. Tsai, Z. Zhu, W. Ren, Y. Luo, S. Carr, M. Luskin, E. Kaxiras, and K. Wang, Phys. Rev. Lett. **127**, 166802 (2021).

[7] N. Leconte and J. Jung, 2D Mater. **7**, 031005 (2020).

[8] H. Meng, Z. Zhan, and S. Yuan, Phys. Rev. B **107**, 035109 (2023).

[9] K. Lee, M. I. B. Utama, S. Kahn, A. Samudrala, N. Leconte, B. Yang, S. Wang, K. Watanabe, T. Taniguchi, M. V. P. Altoé, G. Zhang, A. Weber-Bargioni, M. Crommie, P. D. Ashby, J. Jung, F. Wang, and A. Zettl, Sci. Adv. **6**, eabd1919 (2020).

[10] Y. Cao, V. Fatemi, A. Demir, S. Fang, S. L. Tomarken, J. Y. Luo, J. D. Sanchez-Yamagishi, K. Watanabe, T. Taniguchi, E. Kaxiras, R. C. Ashoori, and P. Jarillo-Herrero, Nature (London) **556**, 80 (2018).

[11] J. M. Park, Y. Cao, K. Watanabe, T. Taniguchi, and P. Jarillo-Herrero, Nature (London) **590**, 249 (2021).

[12] Z. Hao, A. M. Zimmerman, P. Ledwith, E. Khalaf, D. H. Najafabadi, K. Watanabe, T. Taniguchi, A. Vishwanath, and P. Kim, Science **371**, 1133 (2021).

[13] X. Li, F. Wu, and S. Das Sarma, Phys. Rev. B **101**, 245436 (2020).

[14] T. Cea, N. R. Walet, and F. Guinea, Nano Lett. **19**, 8683 (2019).

[15] F. Wu, R.-X. Zhang, and S. Das Sarma, Phys. Rev. Res. **2**, 022010(R) (2020).

[16] S. Moriyama, Y. Morita, K. Komatsu, K. Endo, T. Iwasaki, S. Nakaharai, Y. Noguchi, Y. Wakayama, E. Watanabe, D. Tsuya, K. Watanabe, and T. Taniguchi, arXiv:1901.09356.

[17] X. Liu, Z. Hao, E. Khalaf, J. Y. Lee, Y. Ronen, H. Yoo, D. H. Najafabadi, K. Watanabe, T. Taniguchi, A. Vishwanath, and P. Kim, Nature (London) **583**, 221 (2020).

[18] V. H. Nguyen, T. X. Hoang, and J.-C. Charlier, J. Phys. Mater. **5**, 034003 (2022).

[19] J. M. Park, Y. Cao, L.-Q. Xia *et al.*, Nat. Mater. **21**, 877 (2022).

[20] J. Shi, J. Zhu, and A. H. MacDonald, Phys. Rev. B **103**, 075122 (2021).

[21] M. Long, P. A. Pantaleón, Z. Zhan, F. Guinea, J. Á. Silva-Guillén, and S. Yuan, npj Comput. Mater. **8**, 73 (2022).

[22] T. Cea, P. A. Pantaleón, and F. Guinea, Phys. Rev. B **102**, 155136 (2020).

[23] C. L. Tschirhart, M. Serlin, H. Polshyn, A. Shragai, Z. Xia, J. Zhu, Y. Zhang, K. Watanabe, T. Taniguchi, M. E. Huber, and A. F. Young, Science **372**, 1323 (2021).

[24] M. Serlin, C. L. Tschirhart, H. Polshyn, Y. Zhang, J. Zhu, K. Watanabe, T. Taniguchi, L. Balents, and A. F. Young, Science **367**, 900 (2020).

[25] A. L. Sharpe, E. J. Fox, A. W. Barnard, J. Finney, K. Watanabe, T. Taniguchi, M. A. Kastner, and D. Goldhaber-Gordon, Science **365**, 605 (2019).

[26] X. Yang and B. Zhang, ACS Appl. Nano Mater. **4**, 8880 (2021).

[27] H. Bai, H. Bao, Y. Li, H. Xu, S. Li, and F. Ma, Carbon **191**, 28 (2022).

[28] M. Dienwiebel, G. S. Verhoeven, N. Pradeep, J. W. M. Frenken, J. A. Heimberg, and H. W. Zandbergen, Phys. Rev. Lett. **92**, 126101 (2004).

[29] L. Brown, R. Hovden, P. Huang, M. Wojcik, D. A. Muller, and J. Park, Nano Lett. **12**, 1609 (2012).

[30] A. E. Filippov, M. Dienwiebel, J. W. M. Frenken, J. Klafter, and M. Urbakh, Phys. Rev. Lett. **100**, 046102 (2008).

[31] W. Yan, L. Shui, W. Ouyang, and Z. Liu, J. Mech. Phys. Solids **167**, 104972 (2022).

[32] S. Plimpton, J. Comput. Phys. **117**, 1 (1995).

[33] N. Leconte, S. Javvaji, J. An, A. Samudrala, and J. Jung, Phys. Rev. B **106**, 115410 (2022).

[34] K. Hermann, J. Phys.: Condens. Matter **24**, 314210 (2012).

[35] M. Hirano and K. Shinjo, Phys. Rev. B **41**, 11837 (1990).

[36] N. Leconte, Y. Park, J. An, A. Samudrala, and J. Jung, 2D Mater. **9**, 044002 (2022).

[37] S. Carr, C. Li, Z. Zhu, E. Kaxiras, S. Sachdev, and A. Kruchkov, Nano Lett. **20**, 3030 (2020).

[38] J. Shin, Y. Park, B. L. Chittari, J.-H. Sun, and J. Jung, Phys. Rev. B **103**, 075423 (2021).

[39] W. Zhong and D. Tománek, Phys. Rev. Lett. **64**, 3054 (1990).

[40] J.-M. Martin, in *Superlubricity*, edited by A. Erdemir and J.-M. Martin (Elsevier Science B.V., Amsterdam, 2007), pp. 207–225.

[41] X. Chen and J. Li, Carbon **158**, 1 (2020).

[42] M. Peyrard and S. Aubry, J. Phys. C **16**, 1593 (1983).

[43] K. S. Kim, A. L. Walter, L. Moreschini, T. Seyller, K. Horn, E. Rotenberg, and A. Bostwick, Nat. Mater. **12**, 887 (2013).

[44] B. Shi, X. Gan, K. Yu, H. Lang, X. Cao, K. Zou, and Y. Peng, npj 2D Mater. Appl. **6**, 39 (2022).

[45] B. S. Baboukani, P. C. Nalam, and K. Komvopoulos, Front. Mech. Eng. **8** (2022).

[46] D. W. Brenner, O. A. Shenderova, J. A. Harrison, S. J. Stuart, B. Ni, and S. B. Sinnott, J. Phys.: Condens. Matter **14**, 783 (2002).

[47] J. H. Los, J. M. H. Kroes, K. Albe, R. M. Gordillo, M. I. Katsnelson, and A. Fasolino, Phys. Rev. B **96**, 184108 (2017).

[48] N. Leconte, J. Jung, S. Lebègue, and T. Gould, Phys. Rev. B **96**, 195431 (2017).

[49] M. Wen, S. Carr, S. Fang, E. Kaxiras, and E. B. Tadmor, Phys. Rev. B **98**, 235404 (2018).

[50] The CBN_RPA.drip and CBN_LDA.drip potential files to be used with LAMMPS are available at https://github.com/gjung-group/real-space_relaxation_electronic-structure-calculations

and can be used with the input file from the DRIP example folder in the LAMMPS directory.

[51] B. Polyak, USSR Comput. Math. & Math. Phys. **9**, 94 (1969).

[52] R. M. Balabin, J. Chem. Phys. **129**, 164101 (2008).

[53] J. Jung, A. M. DaSilva, A. H. MacDonald, and S. Adam, Nat. Commun. **6**, 6308 (2015).

[54] F. Bonelli, N. Manini, E. Cadelano, and L. Colombo, Eur. Phys. J. B **70**, 449 (2009).

[55] D. Mandelli, I. Leven, O. Hod, and M. Urbakh, Sci. Rep. **7**, 10851 (2017).

[56] X. Gao, M. Urbakh, and O. Hod, Phys. Rev. Lett. **129**, 276101 (2022).

[57] D. Mandelli, W. Ouyang, M. Urbakh, and O. Hod, ACS Nano **13**, 7603 (2019).